

Topological Proximity Effects in Graphene Nanoribbon Heterostructures

Gufeng Zhang,^{1,2} Xiaoguang Li,^{2,3,1} Guangfen Wu,^{1,4} Jie Wang,¹
Dimitrie Culcer,¹ Efthimios Kaxiras,⁵ and Zhenyu Zhang^{1,5}

¹*ICQD, Hefei National Laboratory for Physical Sciences at the Microscale,
University of Science and Technology of China, Hefei, Anhui, 230026, China*

²*State Key Laboratory of Surface Physics and Department of Physics, Fudan University, Shanghai, 200433, China*

³*Department of Physics and Astronomy, University of Tennessee, Knoxville, TN 37996, USA*

⁴*Shenzhen Institutes of Advanced Technology, Chinese Academy of Sciences, Shenzhen, 518055, China*

⁵*School of Applied Science and Engineering, Harvard University, Cambridge, MA 02138, USA*

Topological insulators (TI) are bulk insulators that possess robust chiral conducting states along their interfaces with normal insulators. A tremendous research effort has recently been devoted to TI-based heterostructures, in which conventional proximity effects give rise to many exotic physical phenomena. Here we establish the potential existence of “topological proximity effects” at the interface of a topological graphene nanoribbon (GNR) and a normal GNR. Specifically, we show that the location of the topological edge states exhibits versatile tunability as a function of the interface orientation, as well as the strengths of the interface coupling and spin-orbit coupling in the normal GNR. For zigzag and bearded GNRs, the topological edge state can be tuned to be either at the interface or outer edge of the normal ribbon. For armchair GNR, the potential location of the topological edge state can be further enriched to be at the edge of or within the normal ribbon, at the interface, or diving into the topological GNR. We also discuss potential experimental realization of the predicted topological proximity effects, which may pave the way for integrating the salient functionality of TI and graphene in future device applications.

PACS numbers: 73.22.Pr 03.65.Vf 73.40.-c

I. INTRODUCTION

The discovery of topological insulators (TIs) has revolutionized our understanding of insulating behavior.^{1–11} The appearance of TI behavior is associated with a quantum topological phase transition.^{1,3,12,13} For example, when the spin-orbit coupling (SOC) exceeds a critical strength, a band inversion takes place, rendering the system a topologically nontrivial global property. Topological phase transitions do not involve symmetry breaking, but entail instead a change in the Z_2 topological invariant, which may be regarded as a quantity counting the number of Dirac cones. No local order parameter can be defined for a topological phase transition. Such TI behavior, which is protected against time-reversal invariant perturbations, is a one-particle phenomenon and is the result of SOC: the carriers at the interface between a TI and a normal insulator are massless Dirac fermions with spin-momentum locking. At the same time, the field of TI also provides a unique platform for studying the interplay between strong SOC and electron-electron correlation effects, as manifested by the existence of exotic quantum phase transitions.¹⁴

Accompanied by the presence of TI behaviors, proximity effects in TI heterostructures yield novel phases of matter.^{15–22} Conventional proximity effects do not involve a topological phase transition, and can be described using local order parameters. For example, TI/superconductor heterostructures exhibit a superconducting proximity effect offering the possibility of observing Majorana fermions¹⁵ and the potential realization of non-Abelian topological quantum computing.²³ The quantized electromagnetic response in a TI-

ferromagnetic material heterostructure is due to a topological magnetoelectric effect.^{18,24} Other novel, technologically important properties have also been demonstrated, such as the enhancement of the catalysis process by robust topological surface states in Au-covered TI.¹⁷ TI-based heterostructures are thus ideal systems of fundamental and practical importance.^{15–20} Harnessing the robust topological surface states entails an accurate understanding and control of their spatial location. Recent first-principles studies of three-dimensional (3D) TI/normal insulator heterostructures have demonstrated that the spatial location of the surface state can be shifted to the surface of the normal insulator,^{19,20} and in a certain parameter range can even be shifted back into the TI bulk.¹⁹ Such studies suggest the possibility of a topological phase transition induced in a normal insulator via *topological proximity effects*, signified by the topological surface state leaking out into an adjacent material or moving back into the TI. Therefore, a realistic and highly nontrivial issue to be addressed is the determination of the exact spatial location of the topological surface state.

In this paper, we exploit the richness of topological proximity effects on quantum topological phase transitions in the important material class of graphene heterostructures²⁵ consisting of a topological graphene nanoribbon (GNR) and a gapped normal GNR. Unlike conventional proximity effects, in which a phase transition is accompanied by symmetry breaking measured by a local order parameter, the topological proximity effects introduced here surrounding topological phase transitions do not involve a symmetry breaking process. Instead of a local order parameter, the measurement of such topological proximity effects is the location of the topo-

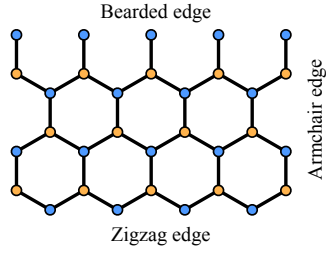


FIG. 1. The schematic of the lattice structures of graphene with zigzag, bearded and armchair edges.

logical edge state (TES), which is determined as a function of the interface coupling strength, the SOC strength in the normal GNR, and the orientation of the interface. We consider three different interface orientations: zigzag, bearded and armchair (shown in Fig. 1), and demonstrate versatile tunability in the location of the TES. For zigzag and bearded²⁶ GNRs, it can be tuned to be either at the interface or the outer edge of the normal GNR. For armchair GNRs, the potential location of the TES is further enriched to be at the edge of or within the normal GNR, at the interface, or diving into the topological GNR.

This paper is organized as follows: In Sec. II, we introduce the tight binding Kane-Mele model for GNR heterostructures. In Sec. III, we show the tunability of TES location as the parameters (interface coupling strength, SOC in the normal GNR) change for zigzag, bearded and armchair GNR heterostructures, which is due to the topological proximity effect. Before concluding in Sec. V, in Sec. IV, we mainly discuss and explain different TES behaviors for different kinds of interface orientations. Potential applications and experimental realizations are also presented.

II. METHODOLOGY

We start with the Kane-Mele model^{1,2} for GNRs, which was one of the first material systems predicted to be a 2D TI. In the present work, we generalize the systems of interest to explore the topological proximity effects in hybrid GNR heterostructures consisting of a normal and a topological GNRs. In these systems, we focus on two central parameters: the tunnel coupling at the interface between the GNRs, and the strength of the SOC in the normal GNR. Potential physical realizations of these systems will be discussed later. We investigate the spatial location of the TES at the interface between the two GNRs for three different interface orientations: zigzag, bearded, and armchair. These three orientations give rise to qualitatively different graphene band structures, and consequently the proximity effects take qualitatively different forms.

For either the topological or normal GNR, we use the same tight-binding Hamiltonian as follows, but with dif-

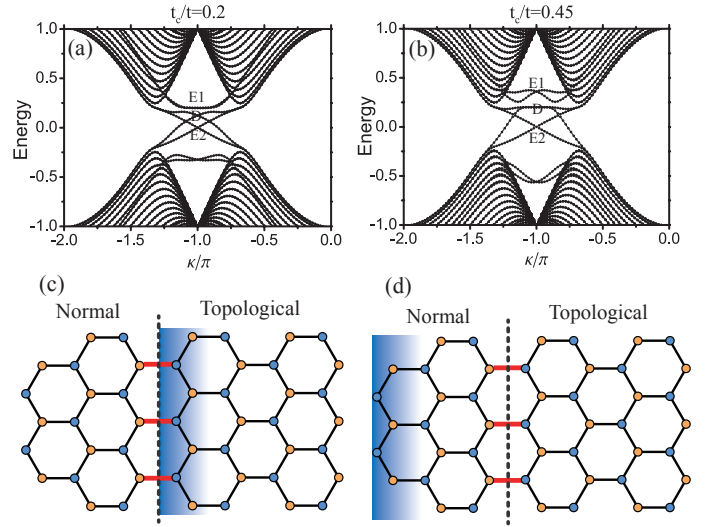


FIG. 2. (Color online) Band structures of zigzag edge GNR heterostructures consisting of a 3-chain normal GNR on the left and a 30-chain topological GNR on the right, shown in (a) and (b) for different tunnel coupling strengths. E_1 and E_2 represent the bands of the trivial edge states originated from the normal GNR. D stands for the Dirac point (crossing of topological edge states). The spatial locations of the D states with higher energy in (a) and (b) are illustrated, respectively, by the blue areas in (c) and (d), where the vertical dotted lines indicate the interface of the heterostructures, and the red bonds show the interface tunnel coupling (t_c). The topological phase transition takes place somewhere between $t_c/t = 0.2$ and $t_c/t = 0.45$.

ferent specifications on the physical parameters:

$$H = t \sum_{\langle ij \rangle} c_i^\dagger c_j + it_2 \sum_{\langle\langle ij \rangle\rangle} c_i^\dagger \boldsymbol{\sigma} \cdot (\mathbf{d}_{kj} \times \mathbf{d}_{ik}) c_j + \sum_{i \in a, b} V_i c_i^\dagger c_i. \quad (1)$$

The first term is the nearest-neighbor hopping term, with the tunnel coupling t and the electron creation (annihilation) operator c_i^\dagger (c_i) on site i . The second term is the intrinsic SOC connecting second-nearest neighbors, where t_2 describes the coupling strength, $\boldsymbol{\sigma}$ is the Pauli matrix vector, i and j are two next-nearest sites, k is the nearest site connecting them, and the vector \mathbf{d}_{ik} points from k to i . The third term is the on-site energy for graphene, with $V_{a(b)}$ for the $A(B)$ sublattice. For the topological GNR, the SOC is set as a constant $t_2 = 0.03t$, and $V_{a(b)} = 0$. For the normal GNR, the SOC is tunable. Other parameters will be specified later.

III. RESULTS

III.1. Zigzag graphene nanoribbon heterostructures

We first investigate GNR heterostructures with zigzag edges. The interface tunnel coupling (t_c) appears as the nearest-neighbor hopping energy between the normal and topological GNRs; it measures the tunable cou-

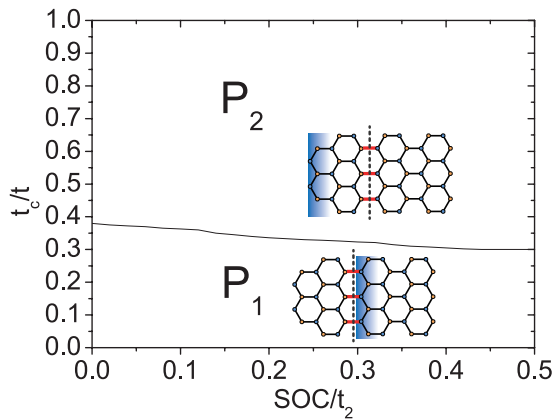


FIG. 3. Phase diagram for the zigzag GNR heterostructures with a 3-chain normal GNR and a 30-chain topological GNR, spanned by the tunnel coupling (t_c) and SOC in the normal GNR. Insets are the schematic illustrations of the spatial locations of the TESs. P_1 phase: the TES is located at the interface. P_2 phase: the TES is located at the outer edge of the normal GNR.

pling at the interface, as indicated by the red bonds in Fig. 2. Originally, the normal zigzag GNR has gapless edge states,²⁷ but one can open a band gap by adding the different on-site energy for the two sublattices. In our first scenario, we set the on-site energy $V_a = -V_b = 0.1t$ and SOC $t_2 = 0$ in the normal GNR, and a tunable t_c between the topological and normal GNRs. The band structures of the systems with different tunnel coupling strengths are given in Figs. 2(a) and 2(b), where we define the “Dirac point” (shown as D) describing the crossing of topological edge states to emphasize the linear dispersion nature around the corresponding k point. The heterostructure consists of a normal GNR on the left, which contains three atomic chains as its width, and a 30-chain topological GNR on the right. In Fig. 2(a), E_1 and E_2 represent the edge states, being separately localized at the two edges of the normal GNR. The two Dirac points corresponds to TESs located at the two edges of the topological GNR. As the tunnel coupling t_c increases, the energy of the E_1 band stays invariable, while the energy of the TES located at interface also increases, until it reaches the energy of E_1 . Then the energy of the Dirac point is locked at this value, while the energy of E_1 starts to increase. The topological phase transition happens when the E_1 and TES bands detach, resulting in a change in the spatial location of the Dirac point as shown in Figs. 2(b) and 2(d). These results show that the dispersion near that Dirac point becomes *flat* and the spatial location of the Dirac point (namely the TES) moves to the outer edge of the normal GNR. No matter how much larger the coupling is further enhanced, the location of the TES will not change after the phase transition.

Qualitatively similar pictures are observed when we include a finite SOC in the normal GNR. Under the influence of both the tunnel coupling and SOC, the system still has two phases. As shown in the phase diagram

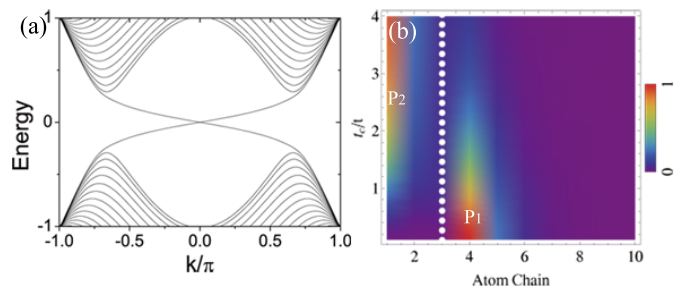


FIG. 4. (Color online) (a) Band structure of a 30-chain bearded edge topological GNR. The Dirac point is located at the Γ point ($k=0$). (b) Phase diagram of the TES location without SOC in the normal GNR. The heterostructures consist of a 3-chain normal GNR on the left and a 30-chain topological GNR on the right. The dotted line indicates the interface of the normal and topological GNRs. P_1 phase: the TES is located at the interface. P_2 phase: the TES is located at the outer edge of the normal GNR.

Fig. 3, the phase transition occurs at the boundary of the P_1 and P_2 areas. Specifically, for given values of t and t_2 , t_c separating the two phases decreases monotonously as the SOC in the normal GNR increases. Furthermore, if the normal ribbon is too wide, the topological proximity effect will not take place, as confirmed with our detailed simulations. In short, two phases exist in a zigzag GNR heterostructure: the TES may be located at the interface or at the outer edge of the normal GNR.

III.2. Bearded graphene nanoribbon heterostructures

We now consider the bearded-edge graphene nanoribbon²⁶ heterostructures. Very similar to zigzag GNR, a pristine bearded GNR has gapless trivial edge states. After turning on the SOC, a Dirac point emerges at the Γ point ($k=0$) [Fig. 4(a)]. The topological phase diagram of the system displayed in Fig. 4 is also very similar to that for zigzag edge heterostructures. As one increases the interface tunnel strength between the heterostructures, the TES moves from the interface (P_1 phase) to the outer edge of the normal ribbon (P_2 phase) [Fig. 4(b)]. Furthermore, switching on the SOC in the normal ribbon still preserve the two phases for the TES.

III.3. Armchair graphene nanoribbon heterostructures

Armchair edge GNR heterostructures differ a lot from both the zigzag and bearded edge GNR heterostructures in that a pristine (e.g. without SOC) armchair GNR does not have trivial edge states.²⁷ We first investigate the spatial location of the TES while keeping the SOC in the normal GNR fixed. The location of the TES as the tunnel coupling increases is given in Fig. 5 with (a) no SOC in the normal GNR and (b) strong SOC ($t_2/t = 0.02$) in the

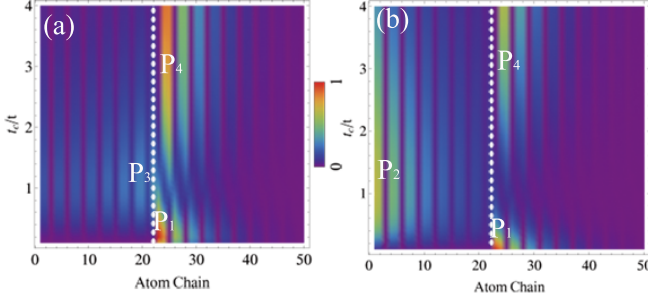


FIG. 5. (Color online) Phase diagram of the TES location for the armchair GNR heterostructures with a 21-chain normal GNR on the left and a 40-chain topological GNR on the right. The SOC strength (t_2/t) is 0.03 in the topological GNR and is 0 (a) or 0.02 (b) in the normal GNR. The on-site energy in the normal GNR is $V_a = -V_b = 0.03t$. The dotted lines indicate the interface location. Four phases appear for the TES as the tunnel coupling (t_c) increases: P_1 phase: the TES is located at the interface; P_2 phase: the TES at the outer edge of the normal GNR; P_3 phase: the TES in the bulk of the normal GNR; P_4 phase: the TES is located one atom chain into the topological GNR.

normal GNR. In contrast with the zigzag and bearded cases, the armchair GNR shows an additional phase in the strong coupling regime, P_4 , where the TES is relocated one atom-chain back inside the topological GNR. On the other hand, with no SOC in the normal GNR (a), the location of the TES shifts from P_1 through P_3 to P_4 as the coupling increases, while for a strong SOC (b), the TES can move to the outer edge of the normal GNR through P_2 instead of P_3 during the evolution. We note that neither the P_3 nor P_4 phase exists for the zigzag or bearded GNR, and the appearance of the P_4 phase is consistent with the *ab initio* work reported recently.¹⁹

Next, we focus on the influence of the SOC in the normal GNR. We study a system consisting of an 8-chain normal GNR connected to a 60-chain topological GNR. The full phase diagram as a function of the tunnel coupling and SOC in the normal GNR is given in Fig. 6. In phase P_1 , the TES is located at the interface, whereas in phase P_4 the TES has moved into the topological GNR by one atom chain. In phase P_2 , the TES has moved to the outer edge of the normal GNR, while in phase P_3 the TES remains in the normal GNR. With strong SOC in the normal GNR and strong tunnel coupling at the interface, the system will remain in the P_2 phase.

IV. DISCUSSION

The movement of the TES to different GNR edges is ascribed to the topological proximity effect. As the interface tunnel coupling becomes stronger, it becomes easier for the SOC on the right side of the junction to leak into the part without SOC, which gives rise to an effective SOC in the normal GNR. However, the phase diagram of

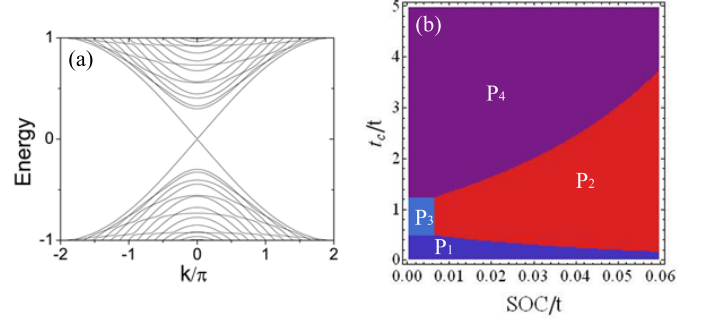


FIG. 6. (Color online) (a) Band structure of a 30-chain armchair edge topological GNR. The Dirac point is at the Γ point. (b) Phase diagram for the armchair GNR heterostructures with an 8-chain normal GNR and a 60-chain topological GNR, spanned by the tunnel coupling and SOC in the normal GNR. The four phases are defined same as in Fig. 5.

the TES locations is different for different orientations of the GNR heterostructures. The existence of the trivial edge states in the case of the zigzag and bearded edges plays an important role in causing this difference. We attribute this difference to the different spatial location of the TES in the overall band structures for the three different systems, at the Γ , Γ , and M points in k space for the armchair, bearded, and zigzag edge GNR, respectively (Figs. 2,4,6). For the zigzag (bearded) edge GNR, the $M(\Gamma)$ points in k space are energetically far away from the bulk states. Correspondingly, in real space, the state at the $M(\Gamma)$ points is an edge state that cannot mix with the bulk states, thereby ruling out the existence of the P_3 and P_4 phases. However, for the armchair edge GNR, the Γ point represents the TES and the energy of the Γ point is close to the bulk bands. As a consequence, it is possible for the TES to interact with the bulk states and move into the bulk. The existence of the two more TES spatial locations in the bulk of the armchair GNR heterostructure represented by P_3 and P_4 confirms this argument.

In short, the relative role of the tunnel coupling and SOC depends on the edge orientation of the GNR heterostructures. For the zigzag and bearded edge GNR, the tunnel coupling is the dominant factor driving the topological proximity effect. At the same time, the SOC helps to make it easier for the TES to propagate to the edge of the normal GNR. For the armchair edge GNR, the SOC is important in allowing the TES to propagate towards the outer edge of the normal GNR, as shown in Fig. 5. In this case, the interface tunnel coupling is concurrently also important, because it underscores the driving force for the $P_1 \rightarrow P_3(P_2) \rightarrow P_4$ transition.

At this point, it is worthwhile to emphasize that conventional proximity effects involve the order parameter of a broken-symmetry phase of a host material leaking into an adjacent material, which is driven into a broken symmetry state of the host material as well. In the topological proximity effects demonstrated here, modulations of the SOC and interface tunnel coupling shift the bound-

ary between a normal insulator and a TI, accompanied by topological phase transitions. A fascinating feature of the topological proximity effects is the dual-proximity nature: The location of the TES can be switched back and forth between the two materials, including placing the topological phase boundary inside an otherwise structurally homogenous material of the normal insulator or the TI. One can regard a conventional proximity effect as a spatial extension of a broken symmetry state. In contrast, the topological proximity effect refers to inducing chiral surface states in an adjacent material as well as controlling their location, again, without symmetry breaking.

Aside from the conceptual advances, the present study may also offer new opportunities in developing spintronic devices and quantum computing. For example, the systems proposed in this work can be used to induce chiral spin-polarized states in a 2D graphene slab at will, which constitutes an ON/OFF switch based on the TES, and can be regarded as a qubit. Such a switch can be controlled by the SOC or the tunnel coupling. As another example, we can further regard the TES as a current loop, and join a square slab of a topological GNR with a square slab of a normal GNR. Whereas the topological side is always in the ON state, the state of the normal insulator side can be modulated. A spin polarization may then be induced in this qubit by coupling it to a ferromagnet, which would enable control of the quantum anomalous Hall effect, and would also serve as a spin injector into the normal GNR.

Here we briefly discuss potential experimental realization of the topological phase transitions predicted in the present study. We first note that, even though the intrinsic SOC in pristine graphene is commonly known to be quite weak,²⁸ some viable approaches have been proposed to enhance the SOC, such as via impurity-induced sp^3 distortion²⁹ and adsorption of heavy adatoms with stronger SOC.^{30,31} Such efforts make it possible to achieve topological GNR. Secondly, the coupling between

a normal and a topological GNR can be tuned by substrate steps, as demonstrated recently,³² where the resistance from the steps on the SiC substrate was found to rise due to the abrupt variation in potential and doping as the graphene extends over a step. These and other alternative candidate structural systems may therefore provide test grounds for physical realization of the quantum topological phase transitions.

V. CONCLUSIONS

We have demonstrated the existence of topological proximity effects in GNR heterostructures consisting of a normal and a topological GNR under a variety of experimentally relevant circumstances. For different types of edges - zigzag, bearded, and armchair - the location of the TES is a function of the interface tunnel coupling and the SOC strength in the normal GNR, demonstrating a rich quantum phase diagram. These findings pave the way for designing next-generation quantum devices that integrate the functionality of graphene and TI. We also stress that the novel topological proximity effects demonstrated here using the prototypical systems of GNR heterostructures are conceptually also applicable to heterostructures consisting of a normal insulator and a 3D TI.

ACKNOWLEDGMENTS

This work was supported by NSF of China (Grant Nos. 91021019 and 11034006), National Basic Research Program of China (Grant No. 2011CB921801), USDOE (Grant No. DE-FG03-02ER45958), and USNSF (Grant No. 0906025).

- ¹ C. L. Kane, and E. J. Mele, Phys. Rev. Lett. **95**, 226801 (2005).
- ² C. L. Kane, and E. J. Mele, Phys. Rev. Lett. **95**, 146802 (2005).
- ³ B. A. Bernevig, T. L. Hughes, and S. C. Zhang, Science **314**, 1757-1761 (2006).
- ⁴ M. König, S. Wiedmann, C. Brüne, A. Roth, H. Buhmann, L. W. Molenkamp, X. L. Qi, and S. C. Zhang, Science **318**, 766 (2007).
- ⁵ L. Fu, C. L. Kane, and E. J. Mele, Phys. Rev. Lett. **98**, 106803 (2007).
- ⁶ J. E. Moore, and L. Balents, Phys. Rev. B **75**, 121306 (2007).
- ⁷ D. Hsieh, D. Qian, L. Wray, Y. Xia, Y. S. Hor, R. J. Cava, and M. Z. Hasan, Nature **452**, 970-974 (2008).
- ⁸ Y. Xia, D. Qian, D. Hsieh, L. Wray, A. Pal, H. Lin, A. Bansil, D. Grauer, Y. S. Hor, R. J. Cava, and M. Z. Hasan, Nature Phys. **5**, 398-402 (2009).

- ⁹ M. Z. Hasan, and C. L. Kane, Rev. Mod. Phys. **82**, 3045 (2010).
- ¹⁰ X. L. Qi, and S. C. Zhang, Rev. Mod. Phys. **83**, 1057 (2011).
- ¹¹ H. J. Zhang, C. X. Liu, X. L. Qi, X. Dai, Z. Fang, and S. C. Zhang, Nature Phys. **5**, 438-442 (2009).
- ¹² M. Kim, C. H. Kim, H. Kim, and J. Ihm, Proc. Natl. Acad. Sci. U.S.A. **109**, 671 (2011).
- ¹³ Su-Yang Xu, Y. Xia, L. A. Wray, S. Jia, F. Meier, J. H. Dil, J. Osterwalder, B. Slomski, A. Bansil, H. Lin, R. J. Cava, and M. Z. Hasan, Science **332**, 560-564 (2011).
- ¹⁴ D. Pesin, and L. Balents, Nat. Phys. **6**, 376, (2010).
- ¹⁵ L. Fu, and C. L. Kane, Phys. Rev. Lett. **100**, 096407 (2008).
- ¹⁶ T. D. Stanescu, J. D. Sau, R. M. Lutchyn, and S. Das Sarma, Phys. Rev. B **81**, 241310(R) (2010).
- ¹⁷ H. Chen, W. G. Zhu, D. Xiao, and Z. Y. Zhang, Phys. Rev. Lett. **107**, 056804 (2011).

- ¹⁸ X. L. Qi, R. D. Li, J. D. Zang, and S. C. Zhang, *Science* **323**, 1184.
- ¹⁹ G. F. Wu, H. Chen, Y. Sun, X. G. Li, P. Cui, C. Franchini, J. L. Wang, X. Q. Chen, and Z. Y. Zhang, arXiv:1203.6718.
- ²⁰ Q. F. Zhang, Z. Y. Zhang, Z. Y. Zhu, U. Schwingenschlögl, and Y. Cui, *ACS Nano*, **6**(3), pp 2345-2352 (2012).
- ²¹ D. Culcer, *Physica E* **44**, 860 (2012).
- ²² Z. Fang, N. Nagaosa, K. S. Takahashi, A. Asamitsu, R. Mathieu, T. Ogasawara, H. Yamada, M. Kawasaki, Y. Tokura, and K. Terakura, *Science* **302**, 92 (2003)
- ²³ C. Nayak, S. H. Simon, A. Stern, M. Freedman, and S. Das Sarma, *Rev. Mod. Phys.* **80**, 1083 (2008).
- ²⁴ X. L. Qi, T. L. Hughes, and S. C. Zhang, *Phys. Rev. B.* **78**, 195424 (2008).
- ²⁵ O. Shevtsov, P. Carmier, C. Petitjean, C. Groth, D. Carpentier, and X. Waintal, *Phys. Rev. X* **2**, 031004 (2012).
- ²⁶ M. Fujita, K. Wakabayashi, K. Nakada, and K. Kusakabe, *J. Phys. Soc. Jpn.* **65**, 1920 (1996).
- ²⁷ K. Wakabayashi, M. Fujita, H. Ajiki, and M. Sigrist, *Phys. Rev. B.* **59**, 8271 (1999).
- ²⁸ Y. G. Yao, F. Ye, X. L. Qi, S. C. Zhang, and Z. Fang, *Phys. Rev. B* **75**, 041401(R) (2007).
- ²⁹ A. H. Castro Neto, and F. Guinea, *Phys. Rev. Lett.* **103**, 026804 (2009).
- ³⁰ C. Weeks, J. Hu, J. Alicea, M. Franz, and R. Q. Wu, *Phys. Rev. X* **1**, 021001 (2011).
- ³¹ H. Jiang, Z. H. Qiao, H. W. Liu, J. R. Shi, and Q. Niu, arXiv:1204.3276.
- ³² T. Low, V. Perebeinos, J. Tersoff, and Ph. Avouris, *Phys. Rev. Lett.* **108**, 096601 (2012).